Multistable pendula as mechanical analogs of ferroelectricity

Romik Khajehtourian[a], Michael J. Frazier[b], Dennis M. Kochmann[a,*]

[a]*Mechanics & Materials Lab, Department of Mechanical and Process Engineering, ETH Zürich, 8092 Zürich, Switzerland*
[b]*Department of Mechanical and Aerospace Engineering, University of California, San Diego, California 92093, USA*

Abstract

Magnetically-controlled and elastically-coupled multistable pendula are shown to serve as versatile structural analogs of ferroelectric crystals, mimicking atomic-level phenomena of domain patterning, domain nucleation, and Allen-Cahn-type domain wall motion under an applied bias, as found, e.g., in ferroelectric switching. We demonstrate the quantitative analogy with material-level transitions via a homogenized continuum description, including structural-level realizations of temperature and lattice defects. Existing photonic, phononic, and topological metamaterials are thus complemented by a new mechanical analog of the nonlinear dissipative kinetics of structural transformations.

Keywords: multistability; metamaterial; phase transformation; domain walls

1. Introduction

Multistability is a prominent feature across biological, chemical, and physical systems [1–3], in which nonconvex energetic potentials lead to the existence of multiple stable equilibrium states. Observed e.g. during solid-solid phase transformations [4], deformation twinning [5] or ferroelectric switching [6], such a multitude of stable ground states leads to their organization into complex microstructural patterns consisting of homogeneous domains or phases arranged in a compatible manner and separated by domain or phase boundaries. Application of an external bias initiates complex domain kinetics, involving nucleation events and domain boundary migration, which collectively make up the material's time-dependent inelastic behavior at larger scales [7, 8]. Ferroelectricity (i.e., the existence of a spontaneous polarization at the atomic unit cell level, which can be irreversibly switched by bias electric fields [9]) serves as a prime example for intricate nano- and microscale domain evolution, whose macroscale electric hysteresis is key to actuators, sensors, and memory devices [10, 11].

Over the past two decades, metamaterials with extraordinary physical properties due to tailored internal architecture have spurred research in acoustics [13, 14], optics [15], and mechanics [16] with the most recent addition of topological insulators [17]. They all mimic atomic-level physics at the structural scale, and they have been almost exclusively limited to either linear properties or static material performance. Recently, the nonlinear dynamics of bistable structures was exploited for energy harvesting [18, 19] and absorption [20], reconfigurable devices and unidirectional wave motion [21–28], yet implementations remained primarily one-dimensional (1D) or bistable and did not offer a direct material-level analogy.

Here, we present a periodic magneto-mechanical system that reproduces the salient features of solid-solid transformations at the structural level with a focus on ferroelectric crystals (Fig. 1a) – amenable to experimental realization and quantitatively following the Allen-Cahn model frequently used to describe ferroelectric switching.

The fundamental building block is a mechanical pendulum (Fig. 1c), which consists of a massless link of length l and a permanent magnet of mass M and dipole moment $\boldsymbol{m}_\mathrm{p}$ (oriented along the pendulum's axis). In addition to gravity, a multi-welled magnetic potential acts onto the pendulum, which arises from five magnets fixed in the plane at a distance $D > l$ below the pivot. Mimicking tetragonal perovskite ferroelectric ceramics in 2D (Fig. 1b), four symmetric energy wells are created by four identical attracting magnets at positions $\boldsymbol{r}_i = (\pm d, \pm d, -D)$, while an identical but repelling magnet at $\boldsymbol{r}_\mathrm{c} = (0, 0, -D)$ defines the energy barrier in the center (magnetic moments are oriented along the positive x_3-axis, as shown, coordinates measured from the pivot). If we define the polarization $\boldsymbol{p} = (\boldsymbol{I} - \boldsymbol{e}_3 \otimes \boldsymbol{e}_3)\boldsymbol{x}$ as the projection of the pendulum's tip position $\boldsymbol{x}$ onto the plane, then the combined magnetic interactions result in a nonconvex potential $\psi_\mathrm{m}(\boldsymbol{p})$ with four symmetric minima separated by a local maximum (Fig. 1d).

Varying the magnet arrangement controls the multistable on-site potential, enabling the analogy to other structural transitions with a vector-valued order parameter; e.g, rhombohedral ferroelectrics can be characterized by four non-symmetric wells in the $(\boldsymbol{p}_1 + \boldsymbol{p}_2)$-$\boldsymbol{p}_3$-plane [29]. In addition, replacing permanent magnets by electromagnets admits control over the energy landscape and enables the
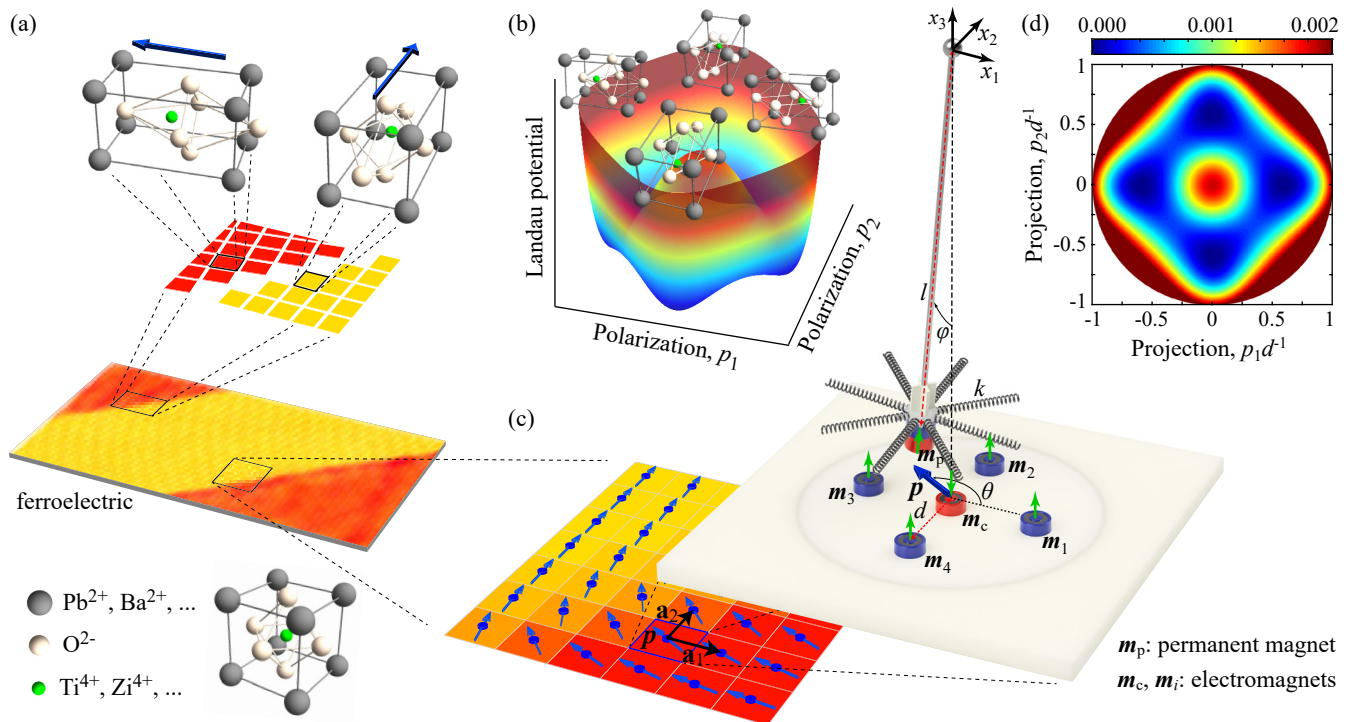

Figure 1: **Multistable mechanical metamaterial as an analog of ferroelectricity**: (a) Drawing inspiration from the perovskite structure of a ferroelectric ceramic (e.g., tetragonal lead-zirconate-titanate) with its atomic-level electric polarization dipole $\boldsymbol{p}$ due to breakage of crystal symmetry and (b) the associated Landau potential [12]. (c) The structural analog: a square lattice of multistable pendula, each elastically connected to its nearest and next-nearest neighbors, with a schematic of the pendulum unit cell detailing the arrangement of magnets, the structural polarization (i.e., 2D projection $\boldsymbol{p}$ of the pendulum position) and the chosen reference frame. (d) The (unbiased) multi-welled potential $\psi(\boldsymbol{p})$ of a single pendulum.

application of bias fields that shift energetic minima and alter barriers (inducing domain switching or promoting phase transitions).

2. Theory

2.1. Magneto-mechanical system

Transitioning from a primitive cell to the effective (single-crystal) behavior, we tessellate the pendulum unit cell on a 2D Bravais lattice, connecting pendulum tips by elastic springs to result in a periodic multistable architecture. Like the magnets controlling the multistable on-site potential, the exact arrangement and connections of pendula control the elastic properties of the effective medium. Consider, e.g., the square lattice in Fig. 1c (defined by basis vectors $\mathbf{a}_1 = a\boldsymbol{e}_1$, $\mathbf{a}_2 = a\boldsymbol{e}_2$) with four nearest-neighbor (NN) and four next-nearest-neighbor (NNN) interactions, so the interaction potential of the ith pendulum is $V_i = \sum_{j=1}^{8} \frac{1}{2} k_j [(\boldsymbol{p} - \boldsymbol{p}_j) \cdot \hat{\boldsymbol{r}}_{ij}]^2$, where $\hat{\boldsymbol{r}}_{ij}$ denotes the unit vector between the pivots of pendulum i and its neighbor j and k_j are the spring stiffnesses, whose values can be tuned to achieve a sought (an)isotropy of the effective medium [30]. We here assume that pendula are sufficiently spaced so all springs undergo approximately linearized (axial) deformation, which simplifies the theory

but does not considerably alter the observed system response.

Unlike its atomic-level counterpart, the pendulum system is of Hamiltonian nature, governed by the deterministic equations of motion based on kinetic energy K and potential energy V:

$$K = \sum_{i=1}^{n} \frac{M}{2} |\dot{\boldsymbol{p}}_i|^2, \quad V = \sum_{i=1}^{n} [V_i(\boldsymbol{p}) + \psi(\boldsymbol{p}_i)].$$

For a long pendulum ($D \gg d$), the gravitational contribution is negligible so the total potential energy is approximately $\psi(\boldsymbol{p}) = \psi_m(\boldsymbol{p}) + \psi_g(\boldsymbol{p}) \approx \psi_{\mathrm{m}}(\boldsymbol{p})$. With the assumption of an effectively 2D motion of the pendulum tip, the gravitational energy is negligible since $\psi_g = Mgl(1 - \cos\phi) \approx 0$ to leading order. The magnetic energy contribution $\psi_m(\boldsymbol{p})$ is

$$\psi_{\mathrm{m}}(\boldsymbol{p}) = \mathbf{m}_{\mathrm{p}} \cdot \left[\mathbf{B}(\mathbf{m}_{\mathrm{c}}, \boldsymbol{r}_{\mathrm{c}} - \boldsymbol{p}) + \sum_{\alpha=1}^{4} \mathbf{B}(\mathbf{m}_\alpha, \boldsymbol{r}_\alpha - \boldsymbol{p}) \right],$$

where the field $\mathbf{B}$ surrounding a magnetic dipole $\mathbf{m}$ in a free space with the permeability of μ_0 is

$$\mathbf{B}(\mathbf{m}, \mathbf{r}) = \frac{\mu_0}{4\pi|\mathbf{r}|^3} \left[\frac{3}{|\mathbf{r}|^2} (\mathbf{m} \cdot \mathbf{r})\mathbf{r} - \mathbf{m} \right].$$

Dissipation is expected primarily from velocity-proportional viscous drag (realized, e.g., by submergence in a fluid or

a pendulum design with significant air drag with effective viscosity β). Lagrange's equation for the ith pendulum with a viscous potential $\mathcal{D} = \beta K/M$, and Lagrangian $\mathcal{L} = K - V$, and externally applied force $\boldsymbol{F}_{\mathrm{ext},i}$ yields the equation of motion

$$\frac{\mathrm{d}}{\mathrm{d}t}\left(\frac{\partial \mathcal{L}}{\partial \dot{\boldsymbol{p}}_i}\right) - \frac{\partial \mathcal{L}}{\partial \boldsymbol{p}_i} + \frac{\partial \mathcal{D}}{\partial \dot{\boldsymbol{p}}_i} = \boldsymbol{F}_{\mathrm{ext},i} \quad \text{for } i = 1,\ldots,n,$$

evaluating to

$$M\ddot{\boldsymbol{p}} + \beta\,\dot{\boldsymbol{p}} + \psi_{\mathrm{m},\boldsymbol{p}}(\boldsymbol{p}) - \sum_{j=1}^{N} k_j[\boldsymbol{e}_j \otimes \boldsymbol{e}_j](\boldsymbol{p}_j - \boldsymbol{p}) = \boldsymbol{F}_{\mathrm{ext}}, \quad (1)$$

where $\boldsymbol{a} \otimes \boldsymbol{b}$ denotes the second-order tensor stemming from the outer product of vectors $\boldsymbol{a}$ and $\boldsymbol{b}$.

Let us consider the periodic pendulum array governed by Eq. (1) as a structural analog of a ferroelectric single-crystal. Akin to an applied bias electric field $\boldsymbol{E}$ in ferroelectrics (which tilts the energy landscape according to $\psi = \psi_{\mathrm{m}} - \boldsymbol{E} \cdot \boldsymbol{p}$), electro-magnets in the plane can actively control the energy landscape of the multistable pendula through an applied electro-magnetic bias (Fig. 2a).

2.2. Continuum limit

To understand the effective, homogenized system response, we pass to the limit of a large array of pendula. We assume a separation of scales between the size of each pendulum unit and the characteristic feature size in the evolving polarization microstructures. This allows us to introduce a continuous polarization field $\boldsymbol{p}(\boldsymbol{x},t)$ which represents the polarization of a pendulum located at position $\boldsymbol{x}$ at time t. To this end, we represent the displacement of the jth adjacent pendulum according to a second-order Taylor expansion:

$$\begin{aligned}\boldsymbol{p}_j(t) = \boldsymbol{p}(\boldsymbol{x},t) &+ a_j \boldsymbol{F}(\boldsymbol{x},t)\boldsymbol{e}_j \\ &+ \frac{1}{2}a_j^2 \nabla \boldsymbol{F}(\boldsymbol{x},t)(\boldsymbol{e}_j \otimes \boldsymbol{e}_j) + \mathcal{O}(a^3)\end{aligned} \quad (2)$$

in which $\boldsymbol{F} = \nabla \boldsymbol{p}$ and $\nabla \boldsymbol{F}$ are, respectively, the first and second gradient of the polarization field $\boldsymbol{p}$, and $\boldsymbol{a}_j = a_j \boldsymbol{e}_j = \boldsymbol{x}_j - \boldsymbol{x}$ is the vector from $\boldsymbol{x}$ to its jth neighboring pendulum. Insertion of Eq. (2) into Eq. (1) in absence of applied external force leads to

$$\begin{aligned} &M\ddot{\boldsymbol{p}} + \beta\,\dot{\boldsymbol{p}} + \psi_{\mathrm{m},\boldsymbol{p}}(\boldsymbol{p}) - \\ &\sum_{j=1}^{N}\left[k_j(\boldsymbol{e}_j \otimes \boldsymbol{e}_j)\left(a_j(\nabla\boldsymbol{p})\boldsymbol{e}_j + \frac{a_j^2}{2}(\nabla\nabla\boldsymbol{p})\boldsymbol{e}_j \otimes \boldsymbol{e}_j\right)\right] = \boldsymbol{0}.\end{aligned}$$

Due to centro-symmetry of the chosen square lattice, we know that for each neighbor j with $\boldsymbol{e}_j$ there is another neighbor with $-\boldsymbol{e}_j$, so $\sum_{j=1}^{N}\left[k_j(\boldsymbol{e}_j \otimes \boldsymbol{e}_j)(\nabla\boldsymbol{p})\boldsymbol{e}_j\right] = \boldsymbol{0}$. This simplifies the equation of motion to

$$M\ddot{\boldsymbol{p}} + \beta\,\dot{\boldsymbol{p}} + \psi_{,\boldsymbol{p}}(\boldsymbol{p}) - a^2\mathbb{C}\,\nabla\nabla\boldsymbol{p} = \boldsymbol{0},$$

where we introduced the fourth-order tensor

$$\mathbb{C} = \frac{1}{2a^2}\sum_{j=1}^{N} k_j a_j^2 (\boldsymbol{e}_j \otimes \boldsymbol{e}_j \otimes \boldsymbol{e}_j \otimes \boldsymbol{e}_j)$$

and the notation $[\mathbb{C}\,\boldsymbol{\mathcal{T}}]_i = \mathbb{C}_{ijkl}\mathcal{T}_{jkl}$ for the contraction of fourth-order tensor $\mathbb{C}$ with third-order tensor $\boldsymbol{\mathcal{T}}$. Finally, dividing by the area of a pendulum unit, a^2, and exploiting the symmetries of fourth-order tensor $\mathbb{C}$, we arrive at the continuum equation of motion

$$\rho\,\ddot{\boldsymbol{p}} + \gamma\,\dot{\boldsymbol{p}} + \tilde{\psi}_{,\boldsymbol{p}}(\boldsymbol{p}) - \nabla \cdot (\mathbb{C}\,\nabla\boldsymbol{p}) = \boldsymbol{0} \quad (3)$$

with mass density per area $\rho = M/a^2$, a dimensionless viscosity (inverse mobility) $\gamma = \beta/a^2$, and the on-site potential per area $\tilde{\psi} = \psi/a^2$. Assuming the overdamped case of negligible inertia compared to the viscous forces ($\rho \ll \gamma$), the above reduces to an Allen-Cahn-type equation of gradient descent, viz.

$$\gamma\,\dot{\boldsymbol{p}} = \nabla \cdot (\mathbb{C}\,\nabla\boldsymbol{p}) - \tilde{\psi}_{,\boldsymbol{p}}. \quad (4)$$

While the multi-welled $\tilde{\psi}$ is the origin of domain formation, the gradient term represents interfacial energy in regions of varying polarization (e.g., in domain walls), which effectively regularizes the domain pattern formation as classically found in phase field models [31]. The components of fourth-order tensor $\mathbb{C}$ depend on the chosen lattice arrangement and spring connection. One particular case of interest is isotropy, characterized by direction-independent stiffness, or $R_{iI}^{\mathsf{T}}R_{jJ}^{\mathsf{T}}\mathbb{C}_{IJKL}R_{Kk}R_{Ll} = \mathbb{C}_{ijkl} \quad \forall\,\boldsymbol{R} \in \mathrm{SO}(d)$. Generally, (expressing the fourth-order tensor as a matrix using Voigt notation)

$$[\mathbb{C}] = \begin{bmatrix} k_{\mathrm{NN}} + k_{\mathrm{NNN}} & 0 & 0 & k_{\mathrm{NNN}} \\ 0 & k_{\mathrm{NNN}} & k_{\mathrm{NNN}} & 0 \\ 0 & k_{\mathrm{NNN}} & k_{\mathrm{NNN}} & 0 \\ k_{\mathrm{NNN}} & 0 & 0 & k_{\mathrm{NN}} + k_{\mathrm{NNN}} \end{bmatrix},$$

and $k_{\mathrm{NN}} = 2k_{\mathrm{NNN}} = k$ implies isotropy with $\nabla \cdot (\mathbb{C}\,\nabla\boldsymbol{p}) = \frac{k}{2}\nabla^2\boldsymbol{p} + k\nabla(\nabla \cdot \boldsymbol{p})$. Of course, this is a simplifying assumption, and the elastic anisotropy may have an impact on the response of the system. However, we limit our study to isotropy, owing to the reported mild anisotropy of tetragonal PZT also used in simulations [12].

2.3. Energy transport scaling law

For a grounded dissipative/diffusive system, the energy transported via a locally-driven planar domain wall scales linearly with the wave velocity v; the constant of proportionality is defined by the physics of the supporting medium [32]. For a planar domain wall with smooth variations of $\boldsymbol{p}$, Eq. (4) reduces to a 1D nonlinear wave equation which upon substitution of a traveling wave solution $\boldsymbol{p}(\boldsymbol{x},t) = \boldsymbol{p}(\boldsymbol{x} \cdot \boldsymbol{e} - vt) = \boldsymbol{p}(\xi)$ with direction unit vector $\boldsymbol{e}$ becomes

$$-v\gamma\boldsymbol{p}_{,\xi} = \boldsymbol{\varepsilon}\boldsymbol{p}_{,\xi\xi} - \tilde{\psi}_{,\boldsymbol{p}}, \quad (5)$$

3

using index notation and Einstein's summation convention with $\boldsymbol{\varepsilon} = \frac{k}{2}(\boldsymbol{I} + \boldsymbol{e} \otimes \boldsymbol{e})$ for isotropy. (In general $\varepsilon_{ik} = \mathbb{C}_{ijkl}e_j e_l$ for a given direction $\boldsymbol{e}$ represents the acoustic tensor.)

Multiplication of Eq. (5) by $-v\boldsymbol{p}_{,\xi}$ and integrating over the entire ξ-axis leads to

$$v^2\gamma \int_{-\infty}^{+\infty} |\boldsymbol{p}_{,\xi}|^2 \, \mathrm{d}\xi = -v \int_{-\infty}^{+\infty} \boldsymbol{p}_{,\xi} \cdot \boldsymbol{\varepsilon} \boldsymbol{p}_{,\xi\xi} \, \mathrm{d}\xi + v \int_{-\infty}^{+\infty} \boldsymbol{p}_{,\xi} \cdot \tilde{\psi}_{,\boldsymbol{p}} \, \mathrm{d}\xi,$$

in which the first term on the right-hand side vanishes (since $\boldsymbol{p}_{,\xi} \to 0$ as $\xi \to \pm\infty$) and hence simplifies to

$$R = v^2\gamma \int_{-\infty}^{+\infty} |\boldsymbol{p}_{,\xi}|^2 \, \mathrm{d}\xi = v\Delta\tilde{\psi}, \qquad (6)$$

where R represents the total power dissipated by the moving domain wall, which is balanced by the energy release $\Delta\tilde{\psi}$ of the wall (multiplied by the domain wall speed v). The second law of thermodynamics ($R \geq 0$) hence dictates that the driving force (which is proportional to $\Delta\tilde{\psi}$) and speed v of a planar domain wall point in the same direction. From an experimental perspective, Eq. (6) provides a beneficial quantitative relation to extract model parameters from experimental snapshots (the integral in Eq. (6) can be evaluated from the shape of the domain wall, so that, e.g., the inverse mobility γ can be computed from an observed wall speed).

2.4. Stochastic formulation of finite temperature

The time evolution law for the vector field $\boldsymbol{p}$, Eq. (4), is known as the Allen-Cahn equation [33] frequently used in phase-field models for ferroelectrics [34, 35], order-disorder transformations [36], structural transitions [7], and in its stochastic extension for temperature dependence [12]. Strictly speaking, it applies at zero temperature, since thermal effects such as thermal vibrations (which influence the switching kinetics) are neglected. At finite temperature, such thermal noise becomes important [12], which is why the kinetic relation can be extended into the stochastic Allen-Cahn equation

$$\gamma\dot{\boldsymbol{p}} = \nabla \cdot (\mathbb{C}\,\nabla\boldsymbol{p}) - \tilde{\psi}_{,\boldsymbol{p}} + \gamma\boldsymbol{q}, \qquad (7)$$

where the last term represents a stochastic, random noise added to the kinetics in order to introduce the effect of thermal vibrations of atoms as Brownian motion. Its amplitude does not depend on the potential [37] but on the system temperature. The random noise must be uncorrelated in both space and time [38, 39] to avoid any bias in the evolution of $\boldsymbol{p}$, i.e.,

$$\langle \boldsymbol{q}(\boldsymbol{x}, t), \boldsymbol{q}(\boldsymbol{x}', t')\rangle = \sigma^2\delta(t - t')\delta(\boldsymbol{x} - \boldsymbol{x}').$$

We apply the Fokker-Planck equation to the evolution of the noise in order to describe the evolution of the probability distribution of the polarization $\boldsymbol{p}$ [40], which has a steady-state solution in the limit of $t \to \infty$. By applying the fluctuation-dissipation theorem [41], one obtains the standard deviation of the noise term as [12]

$$\sigma \propto \sqrt{\frac{2k_B T}{\gamma}}, \qquad (8)$$

in which T denotes temperature and k_B Boltzmann's constant. This summarizes a strategy to include the influence of thermal vibrations into the modeling of microstructure evolution in ferroelectric ceramics.

To mimic thermal fluctuations at finite temperature, we exploit the electromagnets to further induce a distributed stochastic white noise force $\boldsymbol{F}_{\mathrm{ext}} = \gamma\boldsymbol{q}$ in Eq. (1). We use the Box-Müller sampling method [42] to generate uncorrelated Gaussian white noise $\boldsymbol{y}(t) = \big(y_1(t), y_2(t)\big)$ uniformly distributed on the interval $[0, 1]$, i.e., $y_1(t) = \mathrm{rand}[0, 1]$ and $y_2(t) = \mathrm{rand}[0, 1]$ for each pendulum at each time. We define transformation $\boldsymbol{Z} = (Z_1, Z_2)$ with $Z_1 = \sqrt{-2\log y_1}\cos(2\pi y_2)$ and $Z_2 = \sqrt{-2\log y_1}\sin(2\pi y_2)$ to assure no spatial and temporal correlation. Varying the amplitude of the uncorrelated noise term enables us to qualitatively explore the effects of thermal fluctuations, analogously to Eq. (8), i.e., $\boldsymbol{q} = \sigma\boldsymbol{Z}$. Alternatively, a phase-field model can be thermalized quantitatively, e.g., for a precipitation process in which noise depends on the coarse-graining [43].

3. RESULTS AND DISCUSSION

We consider a periodic representative volume element (RVE) consisting of $n_p \times n_p$ pendula with magnets arranged symmetrically to produce the unbiased energy shown in Fig. 2d). While multistable structures have recently attracted attention [18, 19, 44–46], prior realizations have been limited to either 1D systems [22, 23, 32] or to multistability with a scalar order parameter [30]. The multistable potential of the 2D system presented here naturally leads to the formation of domain patterns, characterized by the polarization $\boldsymbol{p}$ as vector-valued order parameter and induced by applying a bias through the electromagnets (Fig. 2a).

We solve Eq. (1) numerically using finite differences based on the explicit Noh-Bathe integration scheme [47] with periodic boundary conditions. Pendula are $l = 0.5$ m long. Magnets are located at $(D, d) = (0.54, 0.06)$ m with dipole moments $(\boldsymbol{m}_\mathrm{p}, \boldsymbol{m}_\mathrm{c}, \boldsymbol{m}_i) = (1.6, -0.64, 0.5)$ Am^2 to produce an unbiased multi-welled energy landscape, with energy barriers proportional to the Landau potential of tetragonal PZT [12] (see SM [48] for details). Simulations use $M = 0.15$ kg, $k_{NN} = 2k_{NNN} = 3$ Nm^{-1}, and $\beta = 4$ Nsm^{-1}. In the SM [48], we discuss in detail how the geometric and material parameters affect the potential.

In our numerical setup we verify the discrete scaling law of Eq. (6) by calculating

$$R_{\mathrm{disc.}} = \gamma \int_0^L |\dot{\boldsymbol{p}}|^2 \, \mathrm{d}x \approx \gamma \sum_{i=1}^{N_p} a|\dot{\boldsymbol{p}}_i|^2 = v\,\Delta\tilde{\psi} \qquad (9)$$
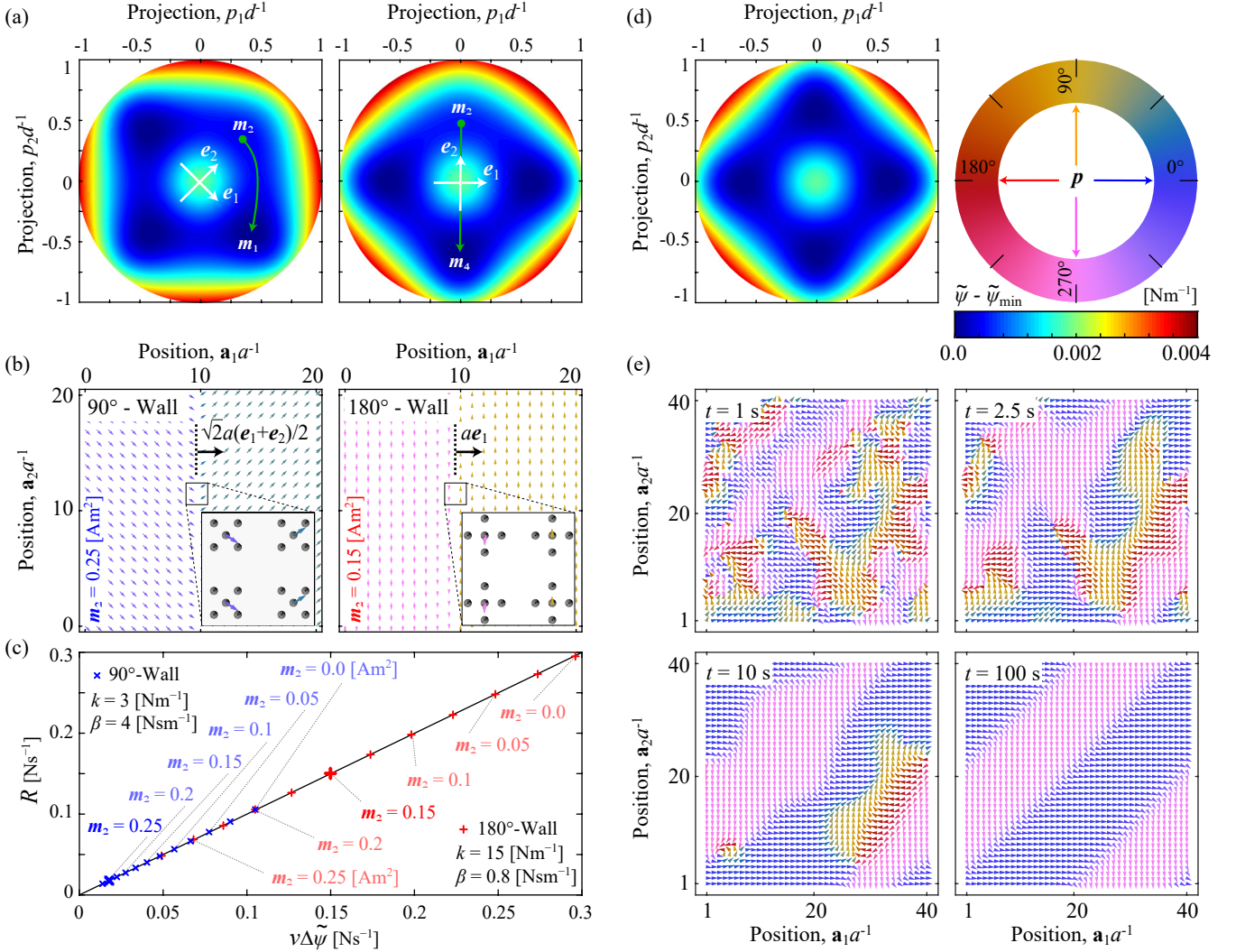
Figure 2: **Domain walls, domain patterns, and domain wall motion**: (a) Biased multi-well potentials for 90° and 180° domain switching, indicating the minimum energy paths. (b) Stationary solution of the polarization distribution near 90° and 180° domain walls (with magnified views of the magnet arrangement). (c) Verification of the energy scaling law of Eq. (6) by numerical simulations. (d) Unbiased multi-well potential. (e) Snapshots of the polarization evolution leading to laminate domain patterns, initiated from a random polarization distribution and featuring charged and uncharged 90° and 180° domain walls and vortices.

for N_{p} lattice sites considered normal to a domain wall (the approximation holds for smooth domain walls of thickness $w \gg a$), while observing the domain wall move at constant speed v under an applied bias differential $\Delta\tilde{\psi}$. Note that Eq. (9) relates the wave quantity R/v linearly to $\Delta\tilde{\psi}$ regardless of domain wall type and propagation direction.

To illustrate the independence of the scaling law of the propagation direction, we examine domain walls traveling along the directions $\mathbf{a}_1 = a\mathbf{e}_1$ and $\mathbf{a}_1 = \sqrt{2}a(\mathbf{e}_1 + \mathbf{e}_2)/2$. Network size and simulation times are ensured sufficient for a steady-state wave (i.e., permanent profile and constant velocity). Fig. 2b shows 180° and 90° domain walls, which are promoted by the bias applied through the electromagnets $\mathbf{m}_i$, as shown in Fig. 2a.

Fig. 2c summarizes simulation data of R vs. $v\Delta\tilde{\psi}$ for moving 180° and 90° domain walls, which confirm the applicability of the scaling relation of Eq. (6). The various

speeds are achieved by altering the magnetic moments $\mathbf{m}_2$ (effectively changing $\Delta\tilde{\psi}$). Discreteness effects manifest for thin domain walls, which is why a sufficient domain wall width is ensured by adjusting the spring stiffness k. Note that, the elastic interaction term does not appear explicitly in the scaling law. However, upon increasing the value of k, the width of the domain wall and consequently the value of R increases (shown in SM [48]), so that domain wall travels faster, which in turn alters v in Eq. (6).

When starting from a random polarization distribution, the simulated system of pendula evolves into a laminate pattern, following Eq. (4) and resulting from the competition between diffusion and stability. Fig. 2e shows four snapshots of a representative time evolution, forming 90° domain walls (see movie SMV1 [48]). Note that the laminate pattern of Fig. 2e depends on the initial random polarization distribution and may change with dif-
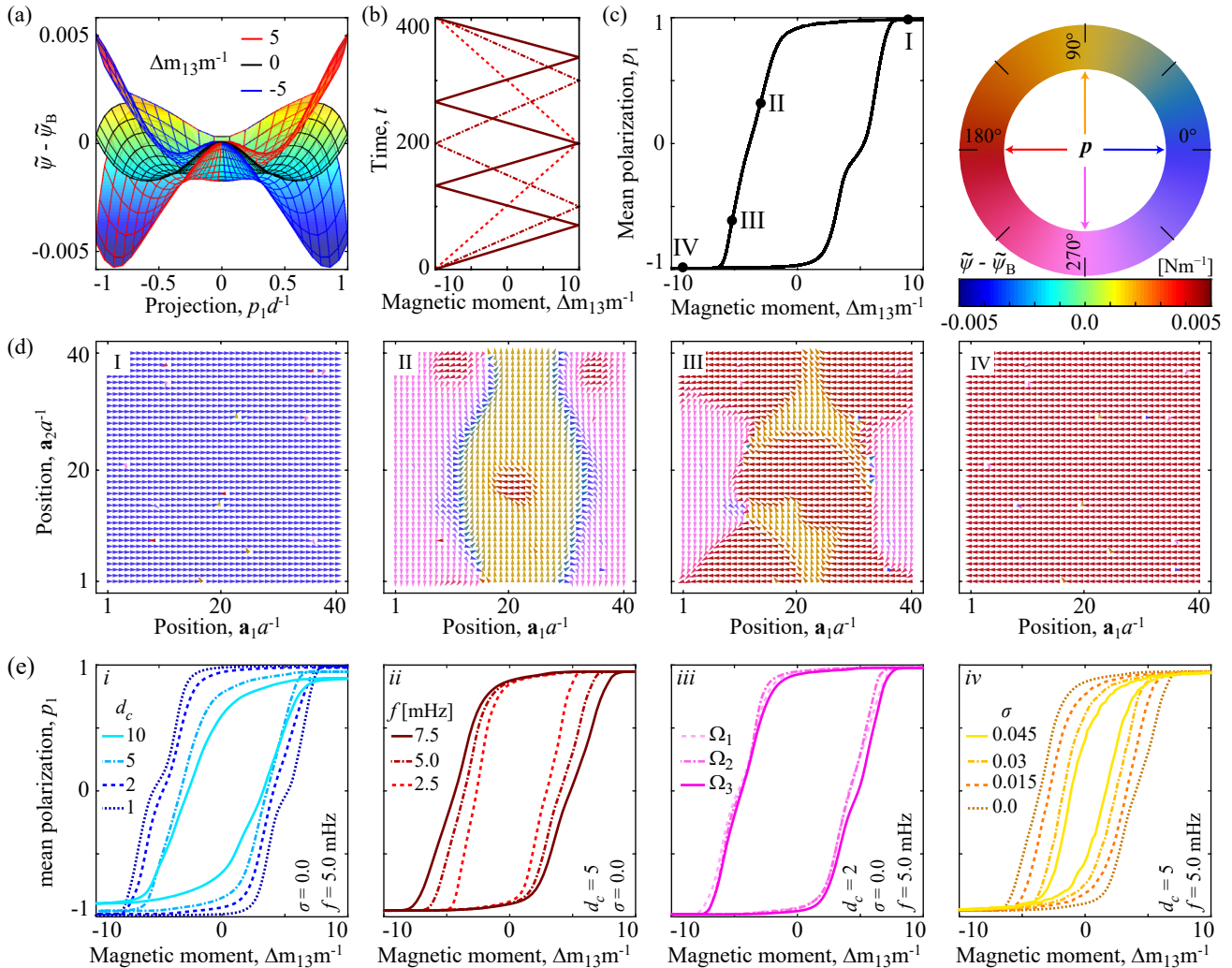
5

Figure 3: **Polarization hysteresis and the influence of defects and 'temperature'.** (a) Biasing the local multi-welled potential along the x_1-direction by changing the magnetic moments $\boldsymbol{m}_1$ and $\boldsymbol{m}_3$ following the triangular wave form in (b). (c) Polarization hysteresis of a 40×40-pendula system with $d_c = 1$ % and $f = 5$ mHz, and (d) snapshots of the evolving polarization distribution showing nucleation near defects and the formation of 90° and 180° domain walls while switching. (e) Effects of (i) defect concentration, (ii) cycling frequency, (iii) defect distribution Ω_i, and (iv) temperature introduced by random noise. Initial distributions vary between samples and specific values of d_c, Ω, σ and f are reported for each case.

ferent random seeds. In the unbiased multi-well potential of Fig. 2c, the 180° energy barrier between two opposing wells is greater than the 90° energy barrier between two neighboring wells, and hence the pendulum system minimizes its energy by forming 90° domain walls. However, for a biased multi-welled potential, the amount of energy required to overcome the central energy barrier may reduce significantly (see Fig. 3a), resulting in the appearance of 180° domain walls (see Fig. 3d).

An important characteristic of ferroelectrics is their hysteresis, which is observed when applying a cycling bias bipolar electric field. The pendulum system reproduces such hysteresis at the structural level, e.g., when cyclically altering the magnetic moments $\boldsymbol{m}_i$ in opposite directions (Fig. 3a). This quasistatic change in the magnetic moments results in a magnetic field that biases the multi-well

potential and consequently affects the polarization of pendula in the RVE.

We apply magnetic moments of triangular waveform in the x_1-direction with amplitude $\Delta m_{ij} = m_i - m_j$ and frequency f (Fig. 3b), which results in the hysteresis of average x_1-polarization vs. applied magnetic moment shown in Fig. 3c. A representative evolving microstructure within the simulated RVE is illustrated in Fig. 3d.

In ferroelectrics, switching is promoted by defects that break the symmetry and cause local hot spots for heterogeneous nucleation. Here, defects are realized by immobile pendula (fixed at their pivots) distributed randomly with a defect concentration $d_c = n_d/n_p^2$ (n_d pendula fixed in their initial polarization per RVE). To assure an unbiased distribution, the net polarization of defects is chosen to vanish. During the microstructural evolution in Fig. 3d, defected

pendula serve as nucleation sites (see movie SMV2 [48]). Fig. 3e illustrates the influence of (i) defect concentration d_c, (ii) cycling frequency f, and (iii) the distribution of defects. As expected from ferroelectrics, the 'coercive field' (magnetic moment at which the polarization switches) and the remnant polarization decrease with increasing d_c and decreasing f and depend marginally on defect distribution.

Aside from re-scaling the Landau potential below the Curie temperature [12], temperature affects ferroelectric switching through thermal fluctuations. In the pendulum system, an externally applied random unbiased noise is implemented through forces on the pendula (q in Eq. (1)). We prevent a macroscopic bias by setting the RVE mean of the noise to 0 and apply a generated Gaussian white noise that is uniformly distributed on the interval $[0, 1]$, uncorrelated in space and time, and having a variance $\sigma^2 \propto k_B T$ with temperature T and Boltzmann's constant k_B [12]. Fig. 3eiv shows how increasing the 'temperature' (i.e., increasing σ) decreases the remnant polarization and the coercive field as observed in ferroelectrics [12].

4. Conclusions

The pendulum system resembles not only qualitatively the multistability of ferroelectric ceramics, but its effective, homogenized behavior reveals a quantitative analogy to phase field models for, among others, ferroelectric ceramics and is hence expected to form characteristic domain patterns involving 90°- and 180°-domain walls. We demonstrate the physics of the pendulum system by numerically solving the discrete equations of motion for selected initial boundary value problems (with experimentally feasible material and geometric parameters).

Of course, the pendulum system – although displaying key features of ferroelectrics (from domain patterns and hysteresis to defect and temperature effects) – cannot reproduce all characteristics of ferroelectric ceramics. For example, the pendula are lacking an analog to Gauss' law, so that no depolarization field exists (which is why charged domain walls are frequently observed). Such an analogous constraint could be implemented through the addition of further springs, effectively imposing a divergence-free condition (see SM [48] for details). Further, the pendulum system lacks electro-mechanical coupling (the RVE size remains unchanged). Yet, the presented system is a quantitative representation of the stochastic Allen-Cahn model for ferroelectrics and serves as a structural analog to material-level nonlinear, dissipative, and diffusive phenomena found, among others, in ferroelectrics and solid-solid phase transformations. Unlike ferroelectrics, all pendulum parameters are freely tunable to adjust the system performance. The pendulum system is hence a rich playground for experimentally realizing and studying material-level phenomena in macroscale structures, with potential for smart and active, multistable mechanical metamaterials.

References

[1] V. K. Wadhawan, Introduction to Ferroic Materials, 1st Edition, CRC Press, 2000, iSBN: 9789056992866.

[2] J. Song, Z. Li, P. Wang, T. Meyer, C. Mao, Y. Ke, Reconfiguration of DNA molecular arrays driven by information relay, Science 357. doi:10.1126/science.aan3377.

[3] L.-Q. Chen, W. Yang, Computer simulation of the domain dynamics of a quenched system with a large number of nonconserved order parameters: The grain-growth kinetics, Phys. Rev. B 50 (1994) 15752–15756. doi:10.1103/PhysRevB.50.15752.

[4] K. Bhattacharya, Microstructure of Martensite, Oxford University Press, Oxford, UK, 2003.

[5] J. W. Christian, S. Mahajan, Deformation twinning, Prog. Mate. Sci. 39 (1-2) (1995) 1–157. doi:10.1016/0079-6425(94)00007-7.

[6] T. Limboeck, E. Soergel, Evolution of ferroelectric domain patterns in batio3 at the orthorhombic tetragonal phase transition, Appl. Phys. Lett. 105 (15) (2014) 152901. doi:10.1063/1.4897361.

[7] A. G. Khachaturyan, Theory of structural transformations in solids, Dover Publications, Dover, UK, 2008.

[8] R. Abeyaratne, J. K. Knowles, Kinetic relations and the propagation of phase boundaries in solids, Arch. Ration. Mech. An. 114 (2) (1991) 119–154. doi:10.1007/BF00375400.

[9] F. Jona, G. Shirane, Ferroelectric Crystals, International Series of Monographs on Solid State Physics, Pergamon press, 1962.

[10] R. E. Newnham, Ferroelectric sensors and actuators: Smart ceramics, in: N. Setter, E. L. Colla (Eds.), Ferroelectric Ceramics, Birkhäuser Basel, Basel, 1993, pp. 363–380.

[11] H. Kohlstedt, Y. Mustafa, A. Gerber, A. Petraru, M. Fitsilis, R. Meyer, U. Bttger, R. Waser, Current status and challenges of ferroelectric memory devices, Microelectronic Engineering 80 (2005) 296 – 304, 14th biennial Conference on Insulating Films on Semiconductors. doi:https://doi.org/10.1016/j.mee.2005.04.084.

[12] R. Indergand, A. Vidyasagar, N. Nadkarni, D. M. Kochmann, A phase-field approach to studying the temperature-dependent ferroelectric response of bulk polycrystalline pzt, J. Mech. Phys. Solids 144 (2020) 104098. doi:10.1016/j.jmps.2020.104098.

[13] M. Maldovan, Sound and heat revolutions in phononics, Nature 503 (2013) 209–217. doi:10.1038/nature12608.

[14] M. I. Hussein, M. J. Leamy, M. Ruzzene, Dynamics of phononic materials and structures: historical origins, recent progress, and future outlook, Appl. Mec. Rev. 66 (2014) 040802. doi:10.1115/1.4026911.

[15] C. M. Soukoulis, M. Wegener, Past achievements and future challenges in the development of three-dimensional photonic metamaterials, Nat. Photonics 5 (2011) 523–530. doi:10.1038/nphoton.2011.154.

[16] J. Christensen, M. Kadic, O. Kraft, M. Wegener, Vibrant times for mechanical metamaterials, MRS Commun. 5 (2015) 453–462. doi:10.1557/mrc.2015.51.

[17] X. Mao, T. C. Lubensky, Maxwell lattices and topological mechanics, Annu. Rev. Conden. Ma. P. 9 (1) (2018) 413–433.

[18] A. F. Arrieta, P. Hagedorn, A. Erturk, D. J. Inman, A piezoelectric bistable plate for nonlinear broadband energy harvesting, Appl. Phys. Lett. 97 (2010) 104102. doi:10.1063/1.3487780.

[19] R. L. Harne, K. W. Wang, A review of the recent research on vibration energy harvesting via bistable systems, Smart Mater. Struct. 22 (2013) 023001. doi:10.1088/0964-1726/22/2/023001.

[20] S. Shan, S. H. Kang, J. R. Raney, P. Wang, L. Fang, F. Candido, J. A. Lewis, K. Bertoldi, Multistable architected materials for

trapping elastic strain energy, Adv. Mater. 27 (29) (2015) 4296–4301. `doi:10.1002/adma.201501708`.

[21] M. Schaeffer, M. Ruzzene, Wave propagation in reconfigurable magneto-elastic kagome lattice structures, J. Appl. Phys. 117 (19) (2015) 194903. `doi:10.1063/1.4921358`.

[22] N. Nadkarni, A. F. Arrieta, C. Chong, D. M. Kochmann, C. Daraio, Unidirectional transition waves in bistable lattices, Phys. Rev. Lett. 116 (24) (2016) 244501. `doi:10.1103/PhysRevLett.116.244501`.

[23] J. R. Raney, N. Nadkarni, C. Daraio, D. M. Kochmann, J. A. Lewis, K. Bertoldi, Stable propagation of mechanical signals in soft media using stored elastic energy, Proc. Natl. Acad. Sci. 113 (35) (2016) 9722–9727. `doi:10.1073/pnas.1604838113`.

[24] Y. Jiang, L. M. Korpas, J. R. Raney, Bifurcation-based embodied logic and autonomous actuation, Nat. Commun. 10 (1) (2019) 128. `doi:10.1038/s41467-018-08055-3`.

[25] L. Jin, R. Khajehtourian, J. Mueller, A. Rafsanjani, V. Tournat, K. Bertoldi, D. M. Kochmann, Guided transition waves in multistable mechanical metamaterials, Proc. Natl. Acad. Sci. 117 (5) (2020) 2319–2325. `doi:10.1073/pnas.1913228117`.

[26] R. Khajehtourian, D. M. Kochmann, Phase transformations in substrate-free dissipative multistable metamaterials, Extreme Mech. Lett. (2020) 100700`doi:10.1016/j.eml.2020.100700`.

[27] R. Khajehtourian, D. M. Kochmann, A continuum description of substrate-free dissipative reconfigurable metamaterials, J. Mech. Phys. Solids (2020) 104217`doi:10.1016/j.jmps.2020.104217`.

[28] R. Khajehtourian, D. M. Kochmann, Soft adaptive mechanical metamaterials, Frontiers in Robotics and AI 8 (2021) 121. `doi:10.3389/frobt.2021.673478`.

[29] P. Lv, Energetics of domain engineered rhombohedral ferroelectric single crystals, Ph.D. thesis (2018).

[30] M. J. Frazier, D. M. Kochmann, Atomimetic mechanical structures with nonlinear topological domain evolution kinetics, Adv. Mater. (2017) 1605800`doi:10.1002/adma.201605800`.

[31] L.-Q. Chen, Phase-field method of phase transitions/domain structures in ferroelectric thin films: A review, J. Am. Ceram. Soc. 91 (6) (2008) 1835–1844. `doi:10.1111/j.1551-2916.2008.02413.x`.

[32] N. Nadkarni, C. Daraio, R. Abeyaratne, D. M. Kochmann, Universal energy transport law for dissipative and diffusive phase transitions, Phys. Rev. B 93 (2016) 104109. `doi:10.1103/PhysRevB.93.104109`.

[33] S. M. Allen, J. W. Cahn, A microscopic theory for antiphase boundary motion and its application to antiphase domain coarsening, Acta Metall. 27 (1979) 1085–1095.

[34] Y. Su, C. M. Landis, Continuum thermodynamics of ferroelectric domain evolution: Theory, finite element implementation, and application to domain wall pinning, J. Mech. Phys. Solids 55 (2007) 280–305. `doi:http://doi.org/10.1016/j.jmps.2006.07.006`.

[35] W. Zhang, K. Bhattacharya, A computational model of ferroelectric domains. Part I: model formulation and domain switching, Acta Mater. 53 (2004) 185–198. `doi:http://doi.org/10.1016/j.actamat.2004.09.016`.

[36] R. W. Balluffi, S. Allen, W. C. Carter, Kinetics of Materials, 1st Edition, John Wiley & Sons, Inc., 2005, iSBN: 9780471246893.

[37] C. Baruffi, A. Finel, Y. Le Bouar, B. Bacroix, O. U. Salman, Overdamped langevin dynamics simulations of grain boundary motion, Materials Theory 3 (1) (2019) 4. `doi:10.1186/s41313-019-0016-1`.

[38] T. Shardlow, Stochastic perturbations of the allen–cahn equation, Electron. J. Differ. Eq. 47 (2000) 1–19.

[39] M. D. Ryser, N. Nigam, P. F. Tupper, On the well-posedness of the stochastic allen–cahn equation in two dimensions, J. Comput. Phys. 231 (6) (2012) 2537–2550. `doi:10.1016/j.jcp.2011.12.002`.

[40] N. G. Van Kampen, Stochastic processes in physics and chemistry, Vol. 1, Elsevier, 1992.

[41] R. Kubo, The fluctuation-dissipation theorem, Rep. Prog. Phys. 29 (1) (1966) 255.

[42] G. E. P. Box, M. E. Muller, A note on the generation of random normal deviates, Ann. Math. Statist. 29 (2) (1958) 610–611. `doi:10.1214/aoms/1177706645`.

[43] Q. Bronchart, Y. Le Bouar, A. Finel, New coarse-grained derivation of a phase field model for precipitation, Physical review letters 100 (1) (2008) 015702.

[44] J. Paulose, A. S. Meeussen, V. Vitelli, Selective buckling via states of self-stress in topological metamaterials, Proc. Natl. Acad. Sci. 112 (2015) 7639–7644. `doi:10.1073/pnas.1502939112`.

[45] D. Restrepo, N. D. Mankame, P. D. Zavattieri, Phase transforming cellular materials, Extreme Mech. Lett. 4 (2015) 52–60. `doi:10.1016/j.eml.2015.08.001`.

[46] D. Yang, L. Jin, R. V. Martinez, K. Bertoldi, G. M. Whitesides, Z. Suo, Phase-transforming and switchable metamaterials, Extreme Mech. Lett. 6 (2016) 1–9. `doi:10.1016/j.eml.2015.11.004`.

[47] G. Noh, K.-J. Bathe, An explicit time integration scheme for the analysis of wave propagations, Comput. Struct. 129 (2013) 178–193. `doi:10.1016/j.compstruc.2013.06.007`.

[48] See supplemental material at [url will be inserted by publisher] for details on the derivation of governing equations in a polar coordinate system, electro-magnet architecture, and ideas for realizing Gauss' law.